Additive Manufacturing 35 (2020) 101195

Contents lists available at ScienceDirect

Additive Manufacturing

journal homepage: www.elsevier.com/locate/addma

Research Paper

Achieving high strength and high ductility in WC-reinforced iron-based composites by laser additive manufacturing

Hongyu Chen[a,b,d], Dongdong Gu[a,b,c,*], Konrad Kosiba[d], Tiwen Lu[d], Liang Deng[d], Lixia Xi[a,b], Uta Kühn[d]

[a] College of Materials Science and Technology, Nanjing University of Aeronautics and Astronautics, Yudao Street 29, Nanjing 210016, Jiangsu Province, PR China
[b] Jiangsu Provincial Engineering Laboratory for Laser Additive Manufacturing of High-Performance Metallic Components, Nanjing University of Aeronautics and Astronautics, Yudao Street 29, Nanjing 210016, Jiangsu Province, PR China
[c] National Key Laboratory of Science and Technology on Helicopter Transmission, Nanjing University of Aeronautics and Astronautics, Yudao Street 29, Nanjing 210016, Jiangsu Province, PR China
[d] Leibniz IFW Dresden, Institute for Complex Materials, P.O. Box 27 01 16, D-01171 Dresden, Germany

ARTICLE INFO

Keywords:
Laser additive manufacturing
Laser powder bed fusion
Iron-based composites
Microstructure
Mechanical properties

ABSTRACT

Strategies for fabricating iron-based materials with high strength and ductility are rare despite intense research efforts within the last decades. This main challenge, which must be overcome in synthesizing such materials, is described by the strength-ductility trade-off dilemma. This study provides a novel approach to achieve the synthesis of highly strong and ductile iron-based composites reinforced with a high weight fraction of WC particles (20 wt%) utilizing laser powder bed fusion (LPBF) as processing technique. Thereby, the LPBF-fabricated composite material has a multi-phase microstructure consisting of ductile austenite (main phase), highly strong martensite and carbidic precipitations extending across different length-scales. The precipitation of (Fe, W)$_3$C type carbide at the Fe/WC interface is well controlled. Thus, a very thin reaction layer (< 500 nm) forms between the WC particles and iron-based matrix. Additionally, nano-scaled precipitations evolve along sub-grain boundaries and within the sub-grains and they show a high coherency with the iron-based matrix. These iron-based composites synthesized by LPBF show an excellent compressive strength of about 2833 MPa and large fracture strain of about 32 %. The following mechanisms contribute to the improved mechanical properties: (1) multiphase material system, (2) grain refinement, (3) substructures, (4) coherent multiscale interfaces and (5) nano-precipitations.

1. Introduction

The incorporation of reinforcements, such as oxides, intermetallic compounds, nitrides, carbides, and borides, into the steel matrix enables the fabrication of materials known as steel matrix composites (SMCs), which bilaterally benefit from the properties of the reinforcement and the matrix [1]. The synthesis of SMCs represents a very effective measure to improve the mechanical properties of steel, such as hardness, strength, fatigue life, and wear resistance [2]. Conventionally, SMCs are prepared using casting or powder metallurgy. These processing routes are time-consuming and challenging to control. Additionally, expensive casting molds, coarse grained microstructure and limited interfacial bonding between reinforcing particles and the matrix pose major challenges in preparing SMCs [3]. Laser powder bed fusion (LPBF) is a popular laser additive manufacturing (LAM) technology enabling the fabrication of complex-shaped components from metals and composites [4]. LPBF permits to synthesize not only iron-based composites with complicated shape, but also with designed microstructures [5]. Therefore, the fabrication of SMCs components by LPBF is recently under intense research and bears great potential for the preparation of novel metallic materials with unprecedented properties.

WC is very suitable as reinforcing particles for Fe-based alloys, because of its high melting point, thermal stability, strength, hardness and good wettability as well as similar coefficient of thermal expansion. Consequently, intensive attempts were conducted to fabricate WC/Fe composites by LPBF within recent years. Thereby, particular focus was on improving the microhardness and wear resistance of LPBF-processed WC/Fe composites, which result from the good adhesion of WC particles through their reaction layer to the Fe-based matrix [6]. However, these works also unraveled challenges in developing high-performance SMCs, like the evolution of thick and also brittle reaction layers between the reinforcing particles and the matrix, due to the formation of

* Corresponding author.

https://doi.org/10.1016/j.addma.2020.101195
Received 31 December 2019; Received in revised form 8 March 2020; Accepted 30 March 2020
Available online 17 May 2020

intermetallic phases, like for instance, M_3C type-carbides [7]. Their formation results in the evolution of cracks, which subsequently propagate along the interface between WC and iron-based matrix [8]. Thus, the WC particles cannot act in a load-bearing manner which is detrimental for the mechanical properties of the composite material. Controlling the phase evolution at the interface between WC reinforcing particles and the iron-based matrix must depend on the diffusion of W, C, Fe and further alloying elements, which is dramatically complex due to the non-equilibrium LPBF-processing. One has to take particular care in controlling the thickness of this reaction layer, so that the WC-particles ensure a good load-bearing effect. The microstructure and strength of WC/Fe composites produced by LPBF have been revealed by Kang et al. [9] who have demonstrated that the addition of WC permits to increase the strength of SMCs not at a large expense on the ductility. However, the strengthening mechanisms of SMCs prepared by LPBF have not been revealed so far, and they can only be understood via a detailed microstructural analysis. Furthermore, one should also investigate how the elements W and C affect the phase transformation of the Fe-based matrix during rapid solidification. W and C greatly extend the range of ferritic and austenitic stability, respectively. Only if the phase formation and resulting microstructure of the SMCs is understood, one can strive for tailoring it in order to ultimately design the mechanical properties of WC/Fe composites by LPBF.

In the present work, WC-reinforced Fe-based composites with high strength and large ductility are prepared via LPBF. In-depth analysis of the phase formation and the resulting microstructure including texture effects on a micrometer scale and precipitations on a nano scale is conducted. Afterwards, we assess the mechanical properties and compare their performance to other Fe-based alloys and composites prepared by different processing technologies. We are convinced that the rapid fabrication of SMCs materials by LPBF bears great potential for the manufacturing of Fe-based components not only with complicated shape, but also with exceptional properties that meet the increasing demand for high performance material in the near future.

2. Experimental procedure

2.1. Powder preparation

Raw materials consisted of gas atomized, spherical 1.2767 L tool steel powder with a mean particle size D50 of 21.6 μm (Fig. 1a), and the polygonal reinforcing WC particles with the equivalent spherical size distribution of 5-15 μm (Fig. 1b). The two powder-types, in which the weight ratio of WC was 20%, were mixed uniformly in a FritschPulverisette6 planetary ball mill (Fritsch GmbH, Germany) using a ball-to-powder weight ratio of 4:1, a rotation speed of the main disc of 200 rpm, and a milling time of 8 h. The well-prepared WC reinforced iron-based composite powder is shown in Fig. 1c. Fig. 1d and e show the energy-dispersive X-ray spectroscopy (EDS) analysis of the location marked by a red cross at the surface of 1.2767 L steel powder. The EDS data of the starting powder will be compared with the one for the LPBF-fabricated composite, so that the variation in chemical composition between original powder material and as-fabricated composite material can be revealed.

2.2. LPBF process

Iron-based composite samples were fabricated in an in-house developed LPBF machine equipped with a YLR-500 ytterbium fiber laser with a maximum power of 500 W and a spot size of 70 μm (IPG Laser GmbH, Burbach, Germany). Furthermore, the in-house built machine consists of an automatic powder layering device, an inert argon gas protection system, and a computer system necessary for the processing control. Optimized laser energy density (laser power P/scan speed v) of 250 ~ 450 J/m was employed to fabricate nearly full-dense samples. The selection of the processing parameters is inferred from our previous work [7]. The layer thickness was set to 30 μm. Cubic samples (10 × 10 × 10 mm^3) and cylindrical samples (∅3 mm, length 6 mm) were produced along the building direction to carry out an in-depth characterization of microstructure and resulting mechanical properties of the LPBF-fabricated iron-based composites.

2.3. Metallurgical defect analysis

The density of the LPBF-fabricated specimens was measured according to the Archimedes principle and computed X-ray tomography (μ-CT, phoenix nanotom m, GE) was used to determine the pore-size distribution. LPBF samples with the highest relative density were selected in order to conduct more detailed characterizations.

2.4. Microstructural characterization

Phase identification was performed on polished composite samples with a thickness of about 1 mm by X-ray diffraction (XRD; STOE Stadi P, Co $K_{\alpha 1}$ radiation) at 40 kV and 40 mA, using a continuous scan type with a step size of 0.02° and scanning speed of 0.5°/min. All XRD scans were conducted on the plane parallel to the LPBF building direction. The microstructure of the LPBF-processed composite samples was characterized using a field emission scanning electron microscope (SEM; Leo 1530 Gemini) equipped with energy-dispersive X-ray spectroscopy (EDS; Quantax400 with SDD-Detector Xflash4010, Bruker). A FEI Tecnai G2 F20 transmission electron microscope (TEM; FEI, Hillsboro, Oregon) was used to conduct high angle annular dark field (HAADF), bright-field (BF), dark-field (DF), energy dispersive spectrometer (EDS) and selected area electron diffraction (SAED) analyses operated at 200 kV with a point-to-point resolution of ≤ 0.21 nm. Atomic and nano-scale characterization at the phase interface was conducted in the high-resolution TEM (HR-TEM) mode. The TEM samples obtained from the LPBF-fabricated components were mechanically polished and finally thinned using a Precision Ion Polishing System (Gatan PIPS™). Phase distribution, micro-texture and grain boundary distribution were analyzed by electron backscattered diffraction (EBSD) in a NANO SEM 430 (FEI, Hillsboro, Oregon). Inverse pole figures (IPF) maps and pole figures (PF) were obtained from three different directions (BD, TD and ND) at the lateral surface of the LPBF-fabricated cubic sample, where BD corresponds to the building direction, TD to the transverse direction which is parallel to the surface of substance, and ND is the normal direction with respect to the lateral surface of the sample. The scanning step size for the IPF map was set at 0.2 μm. The attained data were analyzed using microstructural data analysis software TSL OIM (Ametek Inc, Berwyn, Pennsylvania). It should be noted that only the data for iron-based matrix was analyzed by TSL OIM and other carbidic phases were filtered out by this software to optimize the EBSD data.

2.5. Mechanical properties

Quasi-static compression tests were conducted on an MTS Landmark 370 (MTS Systems Corporation, USA) with 500 kN capacity in displacement-controlled mode at room temperature. The outer surface of the compression samples was kept untreated after the LPBF process in order to obtain the as-fabricated compression properties. To decrease or eliminate any frictional eff ;ects, the top and bottom cross-sectional surfaces of the compression test specimens were lubricated using zinc stearate prior to testing. The displacement rate for all compressive experiments was set as 0.2 mm/min by controlling the cross head velocity. At least three samples were tested to ensure the reproducibility of the mechanical properties and, hence, reliable results.

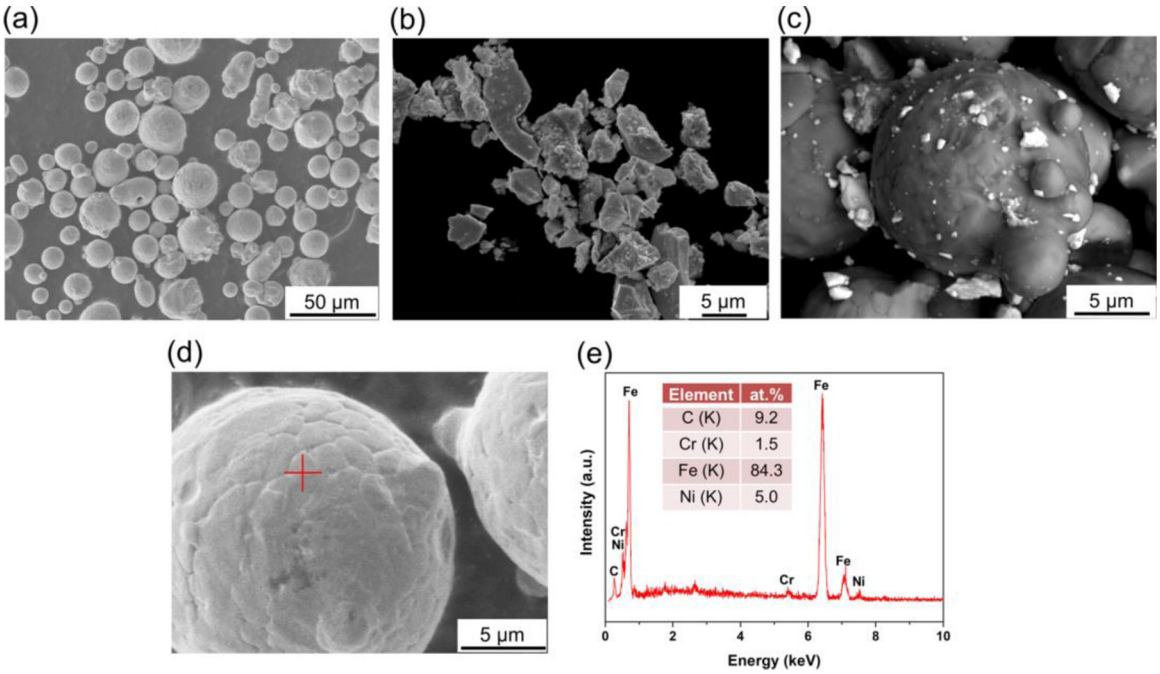

Fig. 1. Morphologies of the initial powders: (a) 1.2767 L tool steel powder; (b) WC particles; (c) Homogeneously mixed Fe-based composite powder reinforced with 20 wt% WC. (d)-(e) The energy-dispersive X-ray spectroscopy (EDS) analysis of the location marked by a red cross at the surface of 1.2767 L steel powder.

3. Results and discussion

3.1. Metallurgical defect analysis

In order to study the dependence of the relative density (RD) on the processing parameters, the distribution of the pore-size inherent to the LPBF-processed composite samples was analyzed using μ-CT. Depending on the processing parameters, altogether three typical defect types of the LPBF-prepared samples can be distinguished by μ-CT and Fig. 2 displays the corresponding reconstructions. The first type of metallurgical sample-defects can be characterized by large irregularly-shaped pores evolving when the laser energy density was set at a low value of 280 J/m. These large pores are distributed throughout the whole sample-volume, resulting in a limited relative density of about 90.48%. With employing higher laser energy density up to 380 J/m, the evolution of large pores was eliminated and only a few extremely small-sized pores can be observed. A high relative density with an overall value of ~99.29% was measured for these samples prepared. The final type of metallurgical defects evolving within the samples during LPBF occurs at an energy density of 440 J/m and can be characterized by the formation and propagation of cracks between the layers. Additionally, some irregular pores could be also observed in the samples synthesized under these processing condition. Consequently, their overall relative density is lower and amounts to a value of only 97.67%. Based on the μ-CT analysis, it was concluded that the samples processed at 380 J/m show the best processing quality, and therefore, these samples were selected for further detailed microstructural characterizations.

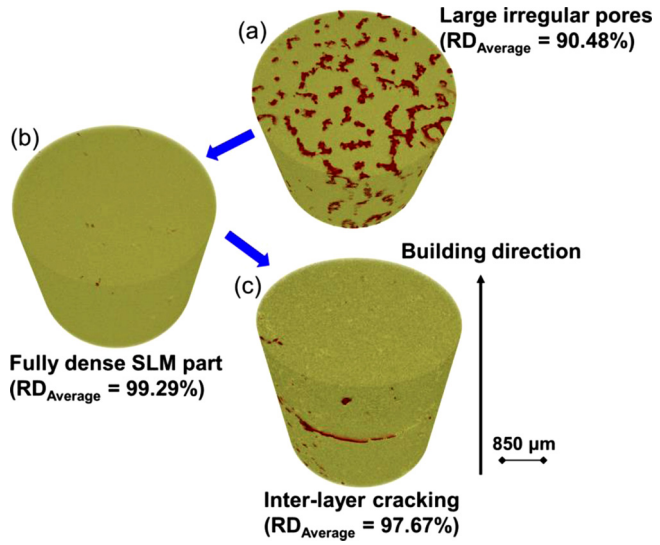

Fig. 2. Evolution of metallurgical defects during LPBF processing of the specimens at three different laser energy densities inferred from μ-CT: (a) 280 J/m, (b) 380 J/m, and (c) 440 J/m.

3.2. Phase identification

A representative XRD pattern of a LPBF-manufactured iron-based composite part prepared at 380 J/m was attained within a wide 2θ range (20-120°) and Fig. 3 displays it. Sharp diffraction reflections corresponding to the face-centered cubic Fe (austenite), tetragonal Fe (martensite) and carbides of the structure-types WC_{1-x} and M_6C were detected. Thereby, austenite is the dominating phase instead of martensite, albeit the fact that, during LPBF-processing tool steel materials, a large proportion of solidified austenite would transform into martensite due to the self-quenching effect [10]. Owing to the presence of WC particles, the austenite phase is stabilized during LPBF, as we will explain in the following. The WC was found to transform into the carbide-type WC_{1-x}, indicating a significant diffusion of carbon from WC particles into the iron-based matrix. This diffusion greatly affects the phase formation of the Fe-based matrix in the direct vicinity of the carbidic reinforcing particles, since carbon is an austenite forming element. We can infer that large amounts of diffused carbon solubilizes in the iron-based matrix as interstitial atoms and affect the phase transformation of the iron-based matrix between austenite and martensite. Moreover, diffused carbon atoms also appear to participate in the formation of the carbide-type M_6C with the carbide forming elements, such as Fe and W.

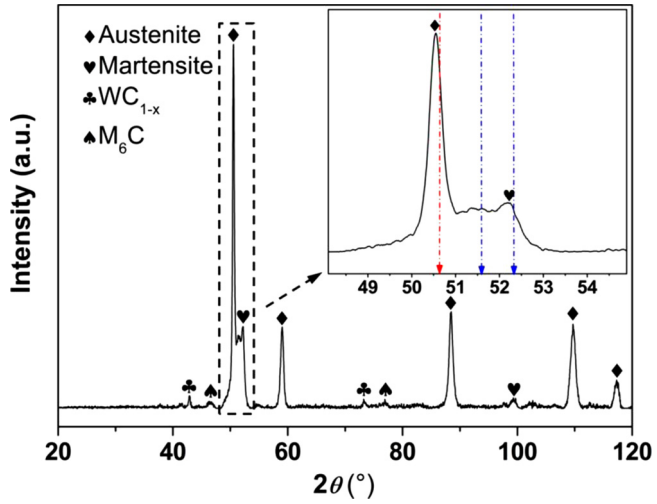

Fig. 3. XRD pattern of the iron-based composite sample. Austenite and martensite as well as carbides of the WC_{1-x} and M_6C types were indexed, where the red and blue dashed lines represent the standard 2θ of austenite and martensite, respectively.

3.3. Microstructural evolution

In order to disclose the phase distribution and micro-texture of the iron-based matrix within the LPBF-processed iron-based composite, an EBSD analysis was conducted parallel to the lateral surface of the prepared samples. The corresponding phase and inverse pole figure (IPF) maps are shown in Fig. 4. From the EBSD results, one can observe that the iron-based matrix composed mainly of austenite instead of martensite. This observation is in line with the results obtained from the XRD analysis. Interestingly, most of the martensitic region is present as a laminar configuration and the corresponding size distribution appears to be bimodal. It seems that the formation of martensite was aggregated at the bottom of the crescent-like molten pool resulting from the laser treatment. It has been well published that the martensitic microstructure generally re-transforms into austenite during the melting of an overlying powder layer, since the temperature in some regions of the molten pool is above the austenite-finish-temperature (A_f), due to the constant heat flow originating from the molten regions towards the building platform [11]. Afterwards, one would expect that austenite transforms into martensite, owing to the high inherent cooling rate effective during LPBF [5]. Therefore, martensite constitutes the major

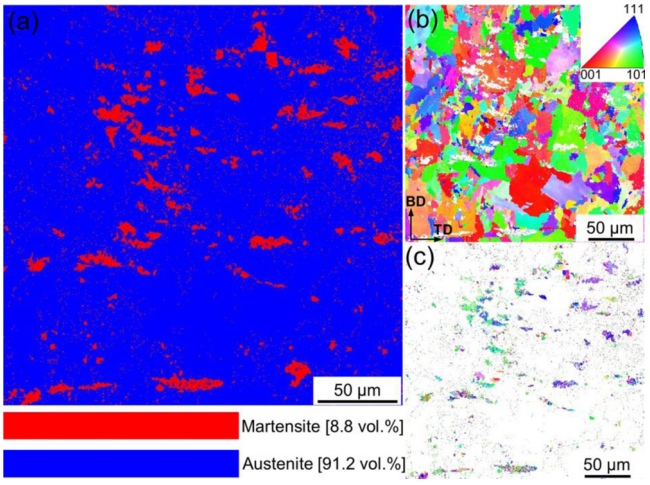

Fig. 4. EBSD analysis shows the phase map (a) and Inverse Pole Figure (IPF) mapping of austenite (b) and martensite (c) within the iron-based matrix (laser energy density = 380 J/m).

phase within the microstructure of LPBF-fabricated tool steels, such as H13 [12]. However, in this study, the majority of the austenite did not transform into martensite during the subsequent cooling process, owing to the presence of WC particles and the resulting diffusion of carbon into the Fe-based matrix. Thus, the untransformed austenite in the previously processed layers is stabilized. This is highly similar to the Q&P process [13] in which austenite is stabilized, due to the carbon-supersaturated martensite. There, the martensite located in the bottom region of the molten pool can be only retained, since the temperature at this location does not exceed the A_s-temperature during melting of overlying powder layers. Thus, the incorporation of WC-particles shows great potential to deliberately tailor the strength and ductility of steel materials through adjusting the volume fraction of austenitic and martensitic phases.

In order to study the grain morphologies and crystallographic micro-texture of the austenite and martensite, IPF mapping was carried out along the building direction (BD) and the corresponding pole figures (PF) were obtained. They are presented in Fig. 4 (right) and Fig. 5. As known from literature, the growth direction of grains is always along the BD, since the maximum heat flux from the molten pool is extracted through the material towards the building plate [10]. Especially for austenitic steel, i.e. 316L, the typical epitaxial columnar microstructure generally exhibits an extremely high degree of anisotropy featuring a strong {0 0 1} texture along the BD [14]. Interestingly, with the addition of WC, the typical columnar microstructure cannot be observed and the grains do not grow into the adjacent layers anymore. Instead, the majority of the austenitic and martensitic grains shows random crystallographic orientations. From the orientation map, a continuous change of color, e.g. the red/blue/green regions, was observed, indicating a highly isotropic microstructure. The PF plots shown in Fig. 4 quantify the micro-texture intensities along the three crystallographic direction-families < 001 > , < 101 > and < 111 > with respect to the lateral surface of the fabricated sample. For the martensite, the overall crystallographic micro-texture is low and only a weakly pronounced < 111 > micro-texture can be detected along the normal direction (ND) (Exp. intensity_{max} = 5.2). In contrast to that, for the austenite, all crystallographic directions distribute more uniformly on the PF with lower convergence (Exp. intensity_{max} = 4.4), which confirms the highly isotropic character of the austenitic grains. These results are also corroborated by the IPF mapping (Fig. 4). The EBSD analysis additionally indicates that one can deliberately alter the microstructure of the iron-based matrix by introducing WC particles during LPBF. These small-sized WC particles act as heterogeneous nucleants for the primary equilibrium phases during solidification of the molten pool by providing low-energy-barrier nucleation sites at the solid/liquid interface [15]. From a thermodynamic point of view, less undercooling is necessary to provide sufficient energy which is required to activate nucleation [16]. Consequently, more nuclei, readily characterized by random crystallographic directions, form during the solidification process, ultimately leading to a material with isotropic properties.

After elaborating on the influence of the reinforcing WC-particles on the crystallographic orientation of the iron-based matrix, we will dwell on the substructure grain boundaries of the matrix in the following. In consideration of the formation of a broad range of substructure boundaries, like sub-grain structures, as well as chemical segregations during rapid non-equilibrium solidification [17], the grain boundaries in LPBF-processed iron-based composites were analyzed based on the EBSD maps. Fig. 6 displays the respective grain boundary map inclusive of the distribution of grain size and rotation angle between adjacent grains. In Fig. 6a, the grain boundary-types are indexed with different colors, such as high angle grain boundaries (HAGBs, 15°-180°) are represented by blue lines and low angle grain boundaries (LAGBs, 2°-15°) by green and brown lines. Indeed, low-angle grain boundaries, also known as sub-grain boundaries, form due to dislocation rearrangement. They are not considered as true grain boundaries, in general [18].

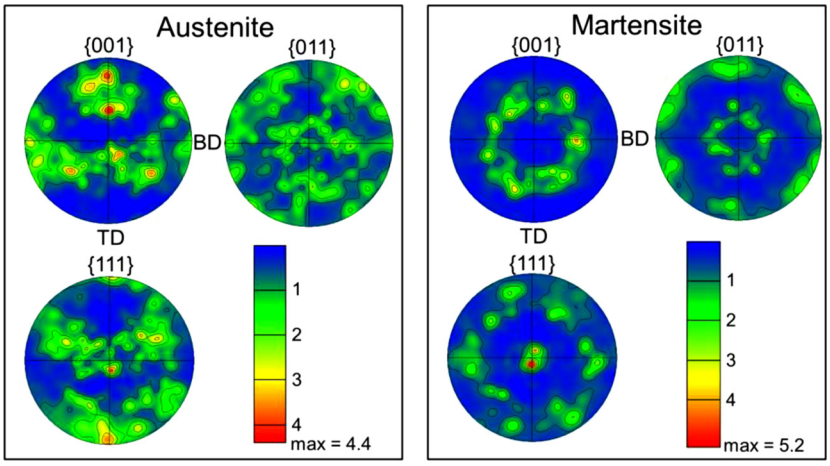

Fig. 5. Pole figure (PF) plots quantify the micro-texture intensities of austenite and martensite along the three crystallographic direction-families < 001 > , < 101 > and < 111 > with respect to the lateral surface of the fabricated samples.

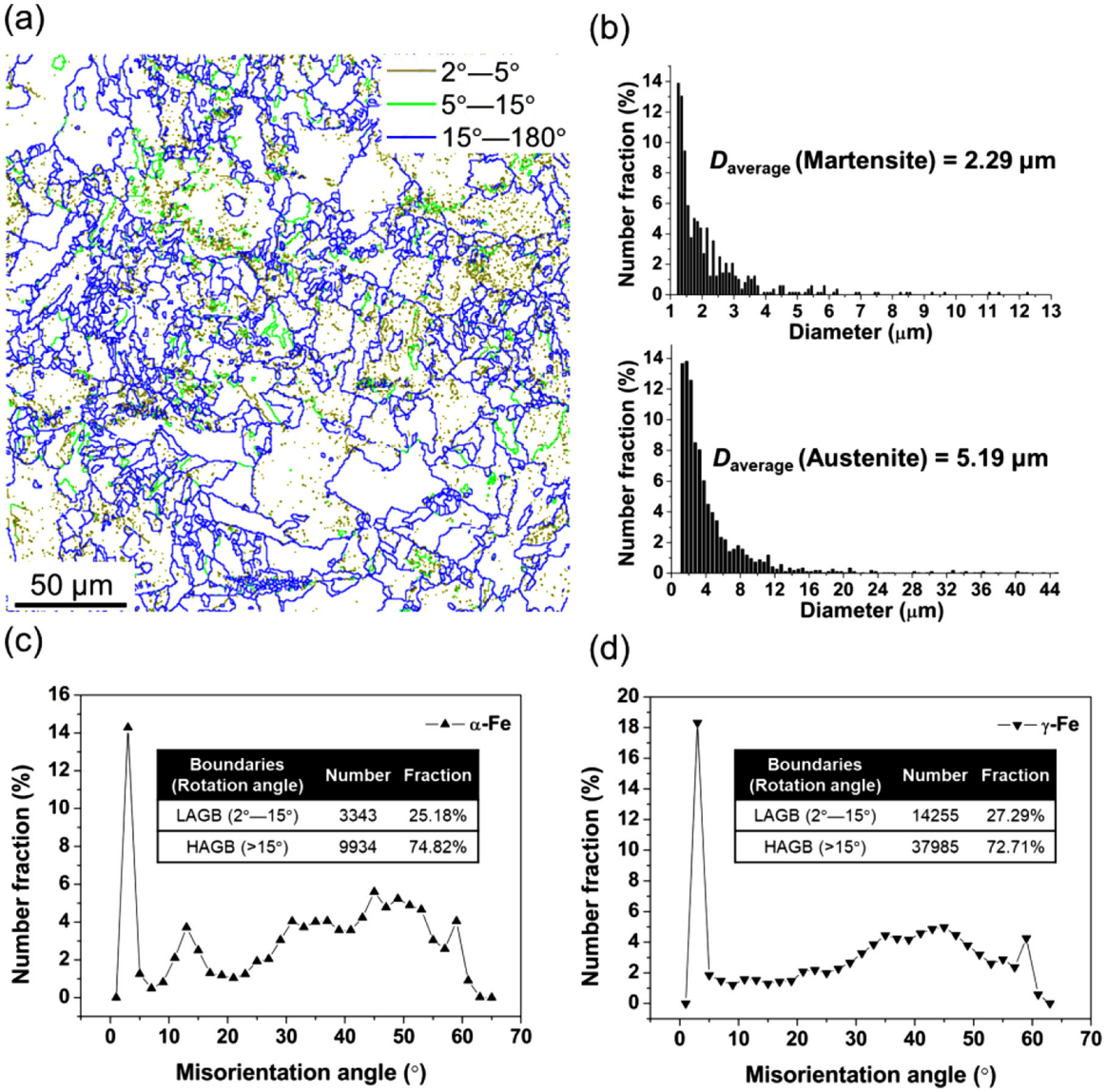

Fig. 6. EBSD analysis shows the (a) grain boundary distribution map, (b) grain size distribution as well as misorientation angle distribution for (c) martensite and (d) austenite in LPBF-processed iron-based composite samples. Thereby, HAGBs are defined with a misorientation angle of 15°-180° and LAGBs are defined with a misorientation angle of 2°-15°.

However, LAGBs cause local lattice distortions and microsegregation effects. Thus, they pose a strengthening mechanism comparable to the strengthening effect caused by HAGBs [17]. The grain size distribution of austenite and retained martensite was measured along the lateral surface of the LPBF-fabricated specimens and it is shown in Fig. 6b. Thereby, the size of the martensitic grains follow a rather bimodal distribution which is in accordance to the results of our previous work, whereby the size of the martensite-packets depends on the location within the molten pool [19]. By contrast, the grain size of the transformed austenite is small (average size of about 5 μm), which is much smaller than the size of austenitic grains of 316L steel synthesized by LPBF (~ 25 μm) [20]. This fact demonstrates the significant grain refinement effect evoked by incorporating WC particles which serve as heterogeneous nucleation sites and, hence hinder the growth of austenitic grains. Fig. 6c and d depict the fraction vs. the misorientation angles of the grain boundary between adjacent grains. Since the formation of martensitic laths always obeys a strict orientation-relationship, their boundaries usually show small misorientations within a block and consist of LAGBs (25.18%), as Fig. 6c illustrates. Martensite packets formed along different habit planes in a primary austenite generally maintain large crystallographic misorientations, entailing the formation of HAGBs (74.82%). For the austenite, similarly, HAGBs constitute the most grain boundaries (72.71%). The LAGBs with a fraction of 27.29% form within the austenite grains as substructures with low misorientation angles. The M_6C type carbides are precipitating at the LAGBs, as will be discussed later on. The microstructure within this iron-based composites reinforced with WC-particles and fabricated by LPBF can be characterized by various features on different length-scales ranging from nano- to microscale. We believe that their interplay and the accompanied crossover is essential for the involved strengthening effect of this composite. Another factor contributing to the high strength of this composite material are the carbidic precipitates and their interfaces which will be addressed next.

FE-SEM and TEM images highlight the morphologies of different carbides present in the LPBF-manufactured Fe-based composites samples (Fig. 7). Since our previous investigation [7] has already confirmed that the WC_{1-x} particles are uniformly distributed within the iron-based matrix at these processing conditions, we only show high-magnification images in this study in order to investigate the interface between the carbidic precipitation and iron-matrix more in detail. During LPBF-processing of the powder mixture consisting of WC- and the Fe-based particles, WC_{1-x} particles result due to the carbon depletion and are well bonded to the matrix (Fig. 7a). The interface is very thin (below 0.5 μm) and consists of a reaction layer. The TEM images show the detailed morphology of the reaction layer (Fig. 7b and c) and selected area electron diffraction (SAED) was conducted to identify the phase constitution of the reaction layer. The reaction layer consists of numerous nano-sized particles. By SAED analysis (Fig. 7f), these nano-particles can be identified as a $(Fe, W)_3C$ type carbide. During LPBF, the concentration of carbon is high in the vicinity of the WC_{1-x} particles (the crystal structure of WC_{1-x} has been proved by SAED in Fig. 7e), due to the strong diffusion effect activated by the high temperature of molten pool. However, the extremely high cooling rate during LPBF force the carbon to undergo a short-distance diffusion, instead of long-distance diffusion. Thus, a very thin reaction layer results. The FE-SEM image shown in Fig. 7d was taken from a region which is not in the direct vicinity of the WC_{1-x} precipitate, where the carbon-diffusion from the WC into the Fe-based matrix is not significant. There, the iron-based matrix consists of fine cellular dendrites and interdendritic primary carbides, which form complex network-like substructures. These interdendritic carbides have compact and lamellar morphologies with a size of 100 to 250 nm in thickness. According to the XRD results, they are carbides of the type M_6C (M = W, Fe, Cr). Aiming to confirm this carbidic type, high angle annular dark field (HAADF) microscopy was endeavored. The corresponding image and EDS map of one cell are illustrated in Fig. 8a. The compositional map reveals a segregation of C and W along the walls of cellular structure. These fine cellular structures are difficult to identify by means of IPF mapping, because these cell walls are formed as LAGBs with very low misorientation angle [17]. Due to the inherent microsegregation effect, these LAGBs are mostly

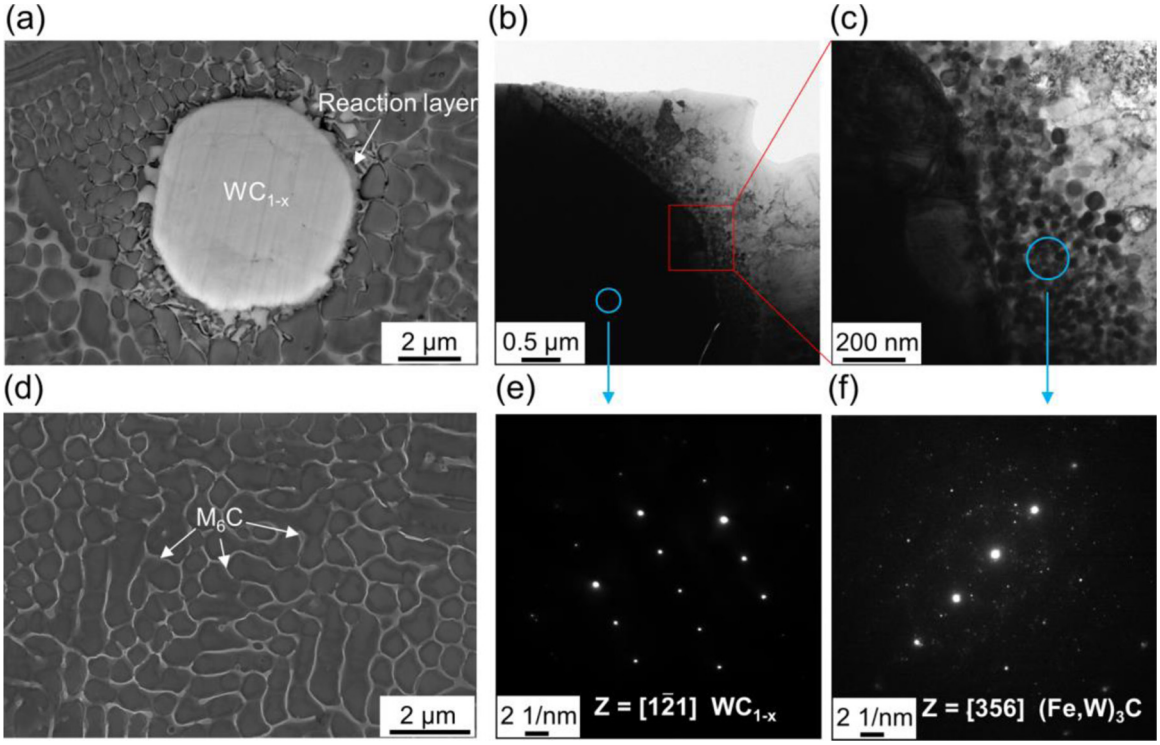

Fig. 7. SEM and TEM images highlight the microstructure (a-c) around the WC_{1-x} phase and (d) within the iron-based matrix not in direct vicinity of the WC_{1-x} phase. (e) and (f) are the selected area electron diffraction (SAED) collected from the indicated region in (b) and (c), respectively (laser energy density = 380 J/m).

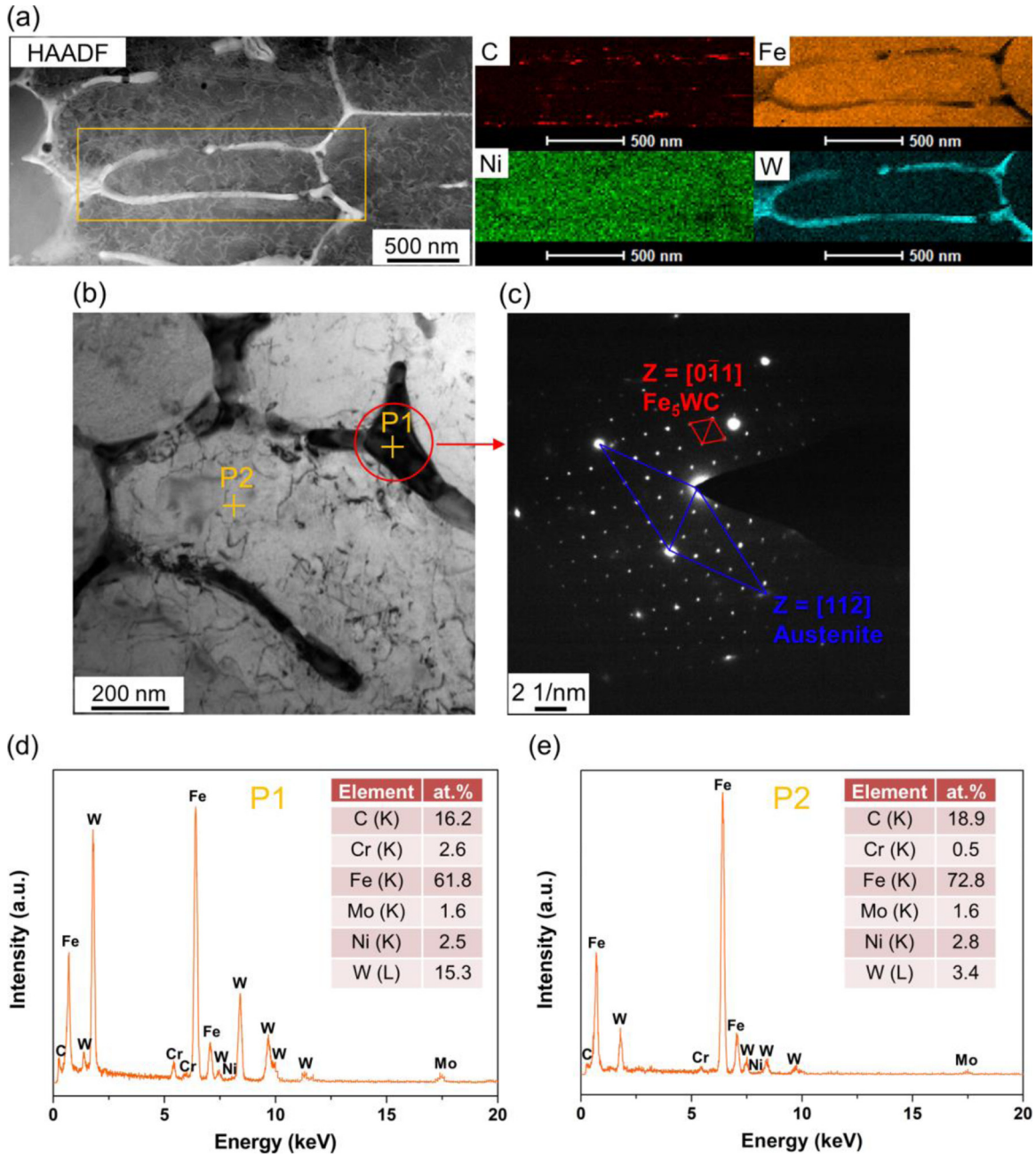

Fig. 8. TEM analysis of the interdendritic carbidic phase. The Fe-based composite was synthesized at a laser energy density of 380 J/m. (a) HAADF TEM image of the solidification cellular structure and related EDS mapping shows the element distribution of C, Fe, Ni and W; (b) BF image shows that the interdendritic carbides are located along the LAGBs and (c) the corresponding SAED pattern collected from the indicated region (red circle) confirms the formation of the Fe_5WC type carbide and retained austenite; (d)-(e) The EDS spectrum was obtained from the location indicated by the orange crosses (Point 1, P1, and Point 2, P2) in (b).

rich in alloying elements, such as the carbide formers Fe, W, and Cr, and hence facilitate the formation of interdendritic carbides. Additionally, TEM-BF was carried out to verify the interdendritic carbidic phase (Fig. 8b), which is located along the LAGBs. The appendant SAED pattern, shown in Fig. 8c, collected from the indicated region (Fig. 8b, red circle) can be indexed as Fe_5WC from the zone axis adopting the face centered cubic space group Fd-3m with a lattice constant of 10.761 Å (red rhombus). Besides, the SAED pattern corresponding to austenite from the <11$\bar{2}$>zone axis can also be observed (blue rhombus). Fig. 8c shows the EDS spectrum of the location marked by the orange cross point 1 (P1) in Fig. 8b. Based on it, one can determine the atomic ratio of Fe, W, and C elements to be close to 5:1:1. This ratio confirms the interdendritic phase to be the Fe_5WC type carbide. According to literature, the interdendritic Fe_5WC carbide has a very low universal anisotropy index of ~0, a high young's modulus of 210.4 GPa as well as a large hardness of 6.01 GPa [21] and its formation is believed to improve the interface cohesion between the sub-grains. Additionally, the interdendritic Fe_5WC carbide could serve as a barrier to the growing and merging sub-grains when subjected to constant heat flux caused by the fabrication of overlying layers via LPBF [22]. Thus, this interdendritic carbidic phase seems to preserve the cross-scaled solidified microstructure of LPBF-fabricated iron-based composite-components. Fig. 8d shows the EDS spectrum of the location marked by the orange cross point 2 (P2) in Fig. 8b. Compared to the EDS result of the original steel powder given in Fig. 1e, one can observe that the C content in the iron-based matrix shows a large increase from 9.2 at.% to 18.9 at.%. It should be noted that it is very difficult to detect the content of C precisely using the EDS analysis because of the contamination of C

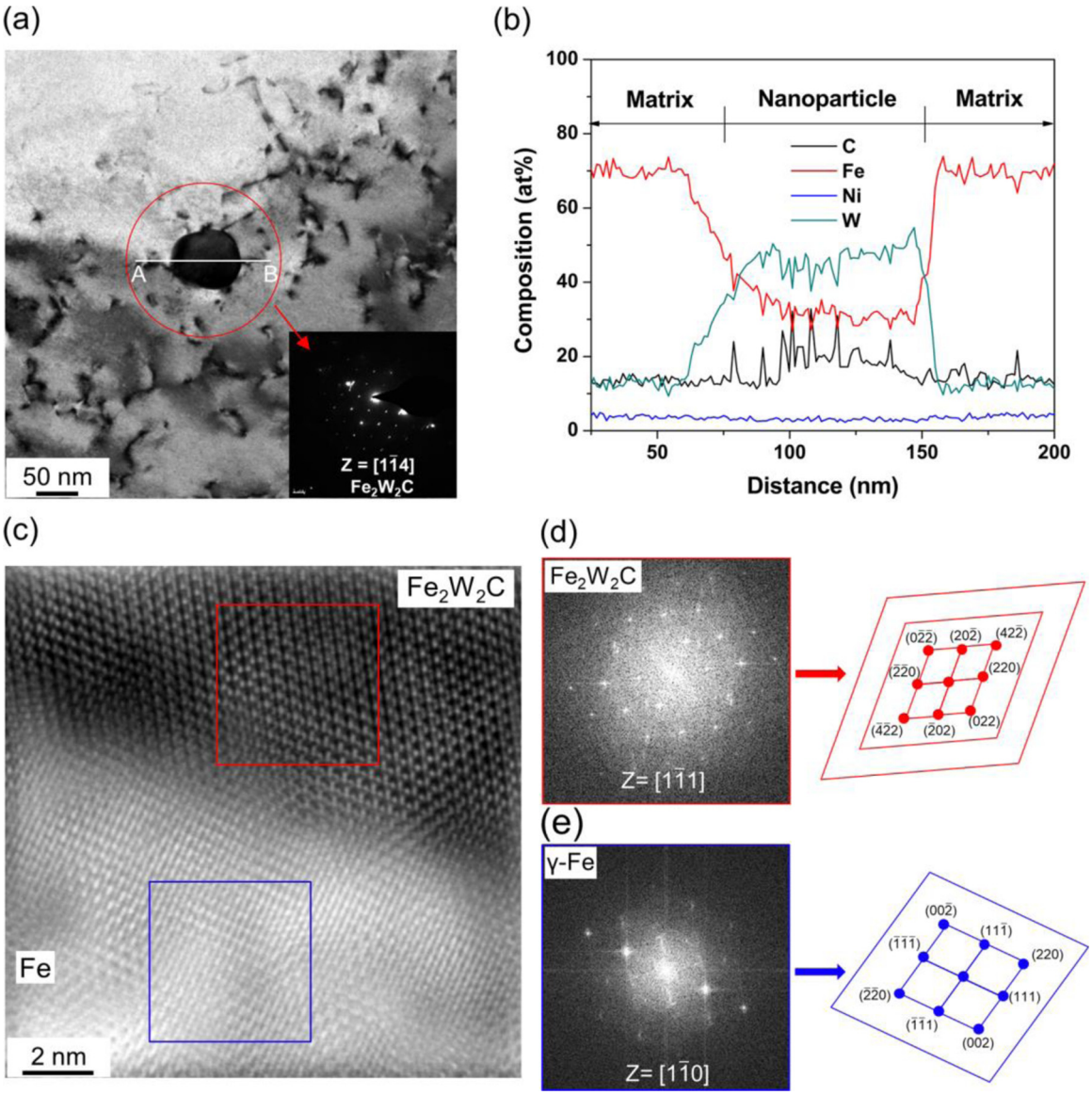

Fig. 9. High-resolution (HR) TEM of a nano-precipitate within the cell substructure. (a) BF image at higher magnification reveals the detailed microstructure inside the cells and the SAED pattern obtained from the indicated region (red circle), shows the formation of a nano-sized Fe_2W_2C precipitation; (b) EDS analysis shows the elemental distribution along the line AB indicated in (a); (c) HR-TEM image under IFFT shows the interface between the nanoparticle and the matrix; (d) FFT pattern of the Fe_2W_2C nanoparticle and (e) the austenitic matrix, oriented to the [1$\bar{1}$1] and [1$\bar{1}$0] zone axes, respectively.

elements or different sensitivities of different elements to the EDS detector. Even so, the significantly increasing trend of C content can prove that the austenite retained during the cooling process of LPBF is due to the diffusion of carbon from WC particles into the Fe-based matrix.

A closer look on the EDS map of carbon shown in Fig. 8a, reveals the carbon to be non-uniformly distributed within the cell substructures, which rises the suspicion of a further carbidic phase to be present inside the sub-grains. Therefore, complementary TEM-BF microscopy was conducted at a higher magnification permitting more detailed microstructural analysis (Fig. 9a). Ultrafine and spherically shaped precipitates with a size of about 70 nm in diameter can be observed. The inset depicts the corresponding SAED pattern allowing to identify this nanoprecipitate as Fe_2W_2C type carbide from the <1$\bar{1}$4> zone axis adopting the face centered cubic space group Fd-3 with lattice constant of 11.105 Å. Additionally, we carried out EDS analysis (Fig. 9b) along a line to determine the variations of C, Fe, Ni and W. The line starts in the Fe-based matrix crosses the nanoprecipitate and ends again within the matrix. Inside the nanoparticle, the atomic ratio of Fe:W was not exactly 1:1, because of inevitable measuring inaccuracies at such a high magnification. The results indicate that the nanoparticle is formed in an environment depleted in solutes such as W and C which have the nominal solution state, when they are not in the direct vicinity of the nanoparticle. This demonstrates that the development of these nanoparticles is mainly based on short-range reshuffling of the constituents instead of long-range diffusion of elements, due to the unique rapid non-equilibrium solidification during LPBF. Fig. 9c presents a high-resolution (HR) TEM image under inverse fast Fourier transformation (IFFT) of the interface between the nanoprecipitate and the surrounding matrix and Fig. 9d and e depict the fast Fourier transformation (FFT) patterns from the regions indicated in Fig. 9c by the red (nanoprecipitate) and blue (matrix) rectangle, respectively. No sharp particle/matrix interfaces can be observed and the nano-sized precipitate appears to be highly coherent with the iron matrix. The FFT patterns further permit to identify the atomic structure of the nanoparticle and Fe-based matrix. The FFT spots confirm that the nanoparticle and Fe-based matrix are indeed of Fe_2W_2C type carbide and austenitic structure. Their relating crystal orientation can be determined as i.e. $[1\bar{1}1]_{Fe2W2C}//[1\bar{1}0]_{Fe}$. These findings are in line with the

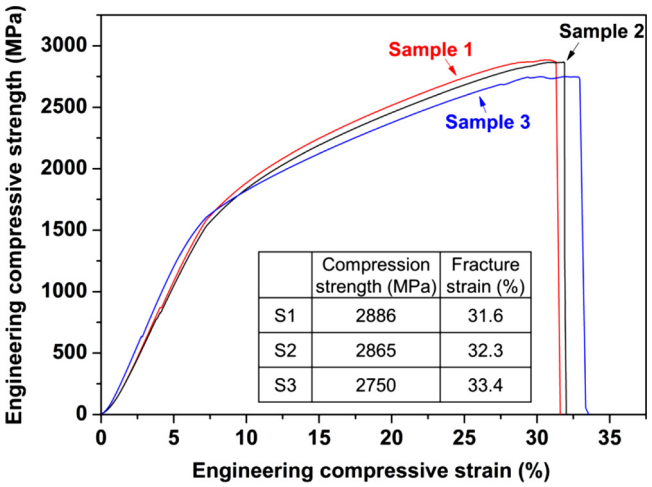

Fig. 10. Three representative engineering compressive stress-strain curves of the LPBF-fabricated iron-based composite. Sample 1 (S1), sample 2 (S2) and sample 3 (S3) were synthesized at the identical processing condition of 380 J/m.

HR-TEM observations. After completing the microstructural analysis of the Fe-based composite, the respective mechanical properties are investigated next.

3.4. Mechanical properties

Three representative compressive engineering stress-strain curves of the iron-based composite processed at 380 J/m are depicted in Fig. 10. All LPBF samples tested demonstrate high compression strengths of about 2800 MPa and a fracture strain under compressive load of about 32%. The mechanical properties of the LPBF-fabricated samples obtained in the present work are compared to other iron-based alloys and composites prepared by different preparation technologies, such as the previously reported FeCrMoVC tool steel, iron-based metallic glass, S390 high-speed steel as well as TiC-, TiB_2-reinforced iron-based composites. Fig. 11 visualizes their fracture strain and compressive strength. The composites, synthesized in this work, show a balanced combination of strength and ductility. Thereby, the fracture strain surpasses the other types of iron-based materials having similar strength. According to literature, the strength and ductility for metal matrix composites can be simultaneously improved via three possible mechanisms: (1) cross-scale grain structure, (2) nanoscale-particles and (3) non-equilibrium grain boundaries, such as sub-grains [23]. As we have demonstrated throughout this work, the microstructure of the Fe-based composite manufactured by LPBF is complex and involves micro- and nanoscopic precipitates as well as substructures and hence fulfills the above-mentioned requirement for manufacturing composites providing both high strength and ductility. We believe that the synergistic interplay between all three microstructural features enables this Fe-based composites to overcome the strength-ductility trade-off dilemma. The multiphase microstructure of this Fe-based composite is composed of high-strength and ductile phases, thus entailing a better combination of strength and ductility. Additionally, the thin reaction layer at the interface between the carbidic particles and the Fe-based matrix is capable of promoting interfacial bonding and stress transfer [24]. Furthermore, the well-dispersed ultrafine interdendritic Fe_5WC carbides contribute to a suppression of grain boundary cracking and avoid interface decohesion during loading [25]. The Fe_2W_2C nano-particles formed inside the subgrains could facilitate the generation of more dislocations during plastic deformation owing to the Orowan mechanism [26]. All these mechanisms appear to cooperate in a synergistic manner, so that the present Fe-based composite shows the desired combination of high strength and large ductility. Nevertheless, to reveal the thorough underlying mechanism for the reinforcement of strength and ductility, a more detailed investigation will be conducted in the near future.

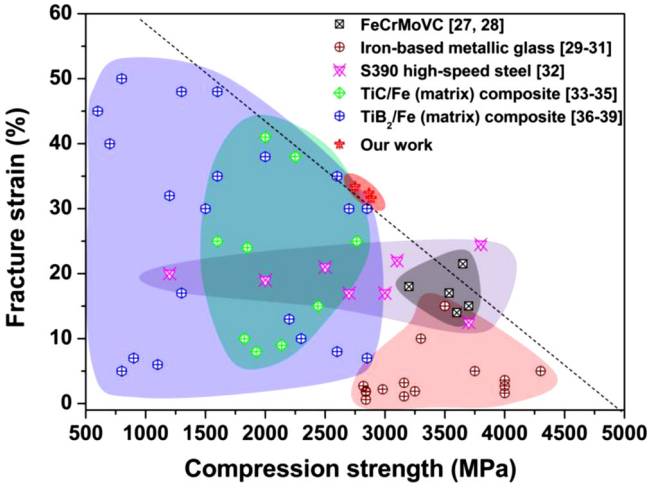

Fig. 11. A comparison between the mechanical properties of the here investigated LPBF-manufactured iron-based composite and other Fe-based alloys as well as their composites fabricated using different techniques [27–39].

4. Conclusions

(1) Introducing WC particles into the iron-based alloy by LPBF significantly influences the phase constitution, since the austenitic phase is stabilized due to the carbon diffusion from the WC reinforcing particles. Thus, the volume fraction of austenite and martensite can be tailored by adjusting the right volume fraction of WC.

(2) The iron-based matrix was characterized as a texture-less microstructure, consisting mainly of fine austenite grains and a small volume fraction of martensite. Small-sized WC particles serve as heterogeneous nuclei for the primary equilibrium phases of the Fe-based alloy, as the molten pool solidifies. The WC-particles provide low-energy-barrier heterogeneous nucleation sites at the solid/liquid interface, so that less energy is necessary to activate nucleation. Consequently, more nuclei form during the solidification process, leading to a more fine-grained and particular isotropic material. During solidification carbon diffused from the WC towards the Fe-based matrix entailing the formation of WC_{1-x} particles and the carbon enriched matrix including a thin reaction layer between both phases with a strong interfacial bonding. The reaction layer consists of numerous nano-sized $(Fe, W)_3C$ carbide particles.

(3) Besides HAGBs, numerous sub-grain could be observed within the Fe-based grains of the matrix, leading to the evolution of diverse substructures within the LPBF-synthesized microstructure. Aside local lattice distortion in matrix-regions, also microsegregations were observed and they arise mainly because of the presence of LAGBs. Along these sub-grain boundaries interdendritic primary carbides of Fe_5WC type precipitate in a network-like structure with an average thickness of 100-250 nm. Additionally, ultrafine spherically shaped carbidic precipitates of Fe_2W_2C type carbide (about 70 nm in diameter) are present at the grain boundaries. These nano-sized carbides showed a highly coherent interface with the iron-based sub-grains, indicative of a strong interfacial bonding. The microstructure of the synthesized Fe-based composite including WC-based reinforcing particles consists of diverse features on completely different length-scales ranging from lower nm to hundreds μm. Thus, one can describes it as a novel cross-scale microstructure which could be only attained by LPBF.

(4) The LPBF-fabricated iron-based composites demonstrate an

excellent compressive strength of about 2833 MPa and simultaneously a large fracture strain of about 32 %. Thus, the synthesized composite material shows a balanced mechanical profile combining high strength and large ductility when compared to other iron-based alloys and composites prepared by different manufacturing technologies. This superior mechanical properties of the LPBF-prepared iron-based composites involve several strengthening mechanisms in a synergistic manner arising from the above described cross-scale microstructural features, such as the multiphase material system, thin particle/matrix reaction layer, grain boundaries strengthening via the refinement of austenite grains and the formation of well-dispersed ultrafine interdendritic Fe_5WC carbides as well as the Orowan mechanism related to the precipitation of Fe_2W_2C nano-particles within the sub-grains.

Declaration of Competing Interest

This paper mainly focused on achieving high strength and high ductility in WC-reinforced iron-based composites by laser additive manufacturing. We declare that we do not have any commercial or associative interest that represents a conflict of interest in connection with the work submitted.

CRediT authorship contribution statement

Hongyu Chen: Methodology, Investigation, Data curation, Writing - original draft. **Dongdong Gu:** Conceptualization, Supervision, Writing - review & editing, Investigation, Data curation. **Konrad Kosiba:** Writing - review & editing, Validation. **Tiwen Lu:** Investigation, Data curation. **Liang Deng:** Investigation, Data curation. **Lixia Xi:** Validation. **Uta Kühn:** Supervision.

Acknowledgements

We are grateful for the financial support from the National Natural Science Foundation of China (No. 51735005); the National Key Research and Development Program “Additive Manufacturing and Laser Manufacturing” (No. 2016YFB1100101); Basic Strengthening Program of Science and Technology (No. 2019-JCJQ-JJ-331); National Natural Science Foundation of China for Creative Research Groups (No. 51921003). K.K. thanks the German Science Foundation (DFG) (grant number: KO 5771/1-1) for financial support.

References

[1] S.C. Tjong, Recent progress in the development and properties of novel metal matrix nanocomposites reinforced with carbon nanotubes and graphene nanosheets, Mater. Sci. Eng. R. Rep. 74 (2013) 281–350.
[2] A.V. Radhamani, H.C. Lau, S. Ramakrishna, CNT-reinforced metal and steel nanocomposites: A comprehensive assessment of progress and future directions, Compos. Part A 114 (2018) 170–187.
[3] B. AlMangour, D. Grzesiak, J.M. Yang, Selective laser melting of TiC reinforced 316L stainless steel matrix nanocomposites: Influence of starting TiC particle size and volume content, Mater. Des. 104 (2016) 141–151.
[4] J. Boes, A. Röttger, L. Becker, W. Theisen, Processing of gas-nitrided AISI 316L steel powder by laser powder bed fusion – Microstructure and properties, Addit. Manuf. 30 (2019) 100836.
[5] S. Pauly, P. Wang, U. Kühn, K. Kosiba, Experimental determination of cooling rates in selectively laser-melted eutectic Al-33Cu, Addit. Manuf. 22 (2018) 753–757.
[6] X.C. Yan, C.Y. Chen, R.X. Zhao, W.Y. Ma, R. Bolot, J. Wang, Z.M. Ren, H.L. Liao, M. Liu, Selective laser melting of WC reinforced maraging steel 300: Microstructure characterization and tribological performance, Surf. Coat. Tech. 371 (2019) 355–365.
[7] D.D. Gu, J. Ma, H. Chen, K. Lin, L. Xi, Laser additive manufactured WC reinforced Fe-based composites with gradient reinforcement/matrix interface and enhanced performance, Compos. Struct. 192 (2018) 387–396.
[8] J.D. Wang, L.Q. Li, W. Tao, Crack initiation and propagation behavior of WC particles reinforced Fe-based metal matrix composite produced by laser melting deposition, Opt. Laser Technol. 82 (2016) 170–182.
[9] N. Kang, W. Ma, L. Heraud, M. El Mansori, F. Li, M. Liu, H. Liao, Selective laser melting of tungsten carbide reinforced maraging steel composite, Addit. Manuf. 22 (2018) 104–110.
[10] J. Zeisig, N. Schädlich, L. Giebeler, J. Sander, J. Eckert, U. Kühn, J. Hufenbach, Microstructure and abrasive wear behavior of a novel FeCrMoVC laser cladding alloy for high-performance tool steels, Wear 382 (2017) 107–112.
[11] M.J. Holzweissig, A. Taube, F. Brenne, M. Schaper, T. Niendorf, Microstructural characterization and mechanical performance of hot work tool steel processed by selective laser melting, Metall. Mater. Trans. B-Proc. Metall. Mater. Proc. Sci. 46 (2015) 545–549.
[12] J.J. Yan, D.L. Zheng, H.X. Li, X. Jia, J.F. Sun, Y.L. Li, M. Qian, M. Yan, Selective laser melting of H13: microstructure and residual stress, J. Mater. Sci. 52 (2017) 12476–12485.
[13] A.J. Clarke, J.G. Speer, M.K. Miller, R.E. Hackenberg, D.V. Edmonds, D.K. Matlock, F.C. Rizzo, K.D. Clarke, E. De Moor, Carbon partitioning to austenite from martensite or bainite during the quench and partition (Q&P) process: A critical assessment, Acta mater. 56 (2008) 16–22.
[14] T. Niendorf, S. Leuders, A. Riemer, H. Richard, T. Tröster, D. Schwarze, Highly anisotropic steel processed by selective laser melting, Metall. Mater. Trans. B 44 (2013) 794–796.
[15] H. Jafarian, J. Habibi-Livar, S.H. Razavi, Microstructure evolution and mechanical properties in ultrafine grained Al/TiC composite fabricated by accumulative roll bonding, Compos. B Eng. 77 (2015) 84–92.
[16] J.H. Martin, B.D. Yahata, J.M. Hundley, J.A. Mayer, T.A. Schaedler, T.M. Pollock, 3D printing of high-strength aluminium alloys, Nature 549 (2017) 365.
[17] Y.M. Wang, T. Voisin, J.T. McKeown, J.C. Ye, N.P. Calta, Z. Li, Z. Zeng, Y. Zhang, W. Chen, T.T. Roehling, R.T. Ott, M.K. Santala, P.J. Depond, M.J. Matthews, A.V. Hamza, T. Zhu, Additively manufactured hierarchical stainless steels with high strength and ductility, Nat. Mater. 17 (2018) 63–71.
[18] B. AlMangour, Y.-K. Kim, D. Grzesiak, K.-A. Lee, Novel TiB2-reinforced 316L stainless steel nanocomposites with excellent room- and high-temperature yield strength developed by selective laser melting, Compos. Part B 156 (2018) 51–63.
[19] H. Chen, D. Gu, D. Dai, C. Ma, M. Xia, Microstructure and composition homogeneity, tensile property, and underlying thermal physical mechanism of selective laser melting tool steel parts, Mater. Sci. Eng. A 682 (2017) 279–289.
[20] A. Röttger, K. Geenen, M. Windmann, F. Binner, W. Theisen, Comparison of microstructure and mechanical properties of 316 L austenitic steel processed by selective laser melting with hot-isostatic pressed and cast material, Mater. Sci. Eng. A 678 (2016) 365–376.
[21] Z.Q. Lv, Z.A. Zhou, S.H. Sun, W.T. Fu, Phase stability, electronic and elastic properties of Fe6-xWxC (x= 0-6) from density functional theory, Mater. Chem. Phys. 164 (2015) 115–121.
[22] J.W. Cahn, Impurity-Drag Effect in Grain Boundary Motion, Acta Metall. 10 (1962) 789–798.
[23] G. Liu, G.J. Zhang, F. Jiang, X.D. Ding, Y.J. Sun, J. Sun, E. Ma, Nanostructured high-strength molybdenum alloys with unprecedented tensile ductility, Nat. Mater. 12 (2013) 344–350.
[24] L.Q. Li, D.J. Liu, Y.B. Chen, C.M. Wang, F.Q. Li, Electron microscopy study of reaction layers between single-crystal WC particle and Ti-6Al-4V after laser melt injection, Acta Mater. 57 (2009) 3606–3614.
[25] X.P. Li, G. Ji, Z. Chen, A. Addad, Y. Wu, H.W. Wang, J. Vleugels, J. Van Humbeeck, J.P. Kruth, Selective laser melting of nano-TiB2 decorated AlSi10Mg alloy with high fracture strength and ductility, Acta Mater. 129 (2017) 183–193.
[26] Z. Zhang, D.L. Chen, Consideration of Orowan strengthening effect in particulate-reinforced metal matrix nanocomposites: A model for predicting their yield strength, Scripta Mater. 54 (2006) 1321–1326.
[27] J. Sander, J. Hufenbach, L. Giebeler, H. Wendrock, U. Kühn, J. Eckert, Microstructure and properties of FeCrMoVC tool steel produced by selective laser melting, Mater. Des. 89 (2016) 335–341.
[28] J. Hufenbach, L. Giebeler, M. Hoffmann, S. Kohlar, U. Kühn, T. Gemming, S. Oswald, B. Eigenmann, J. Eckert, Effect of short-term tempering on microstructure and mechanical properties of high-strength FeCrMoVC, Acta Mater. 60 (2012) 4468–4476.
[29] M. Stoica, J. Eckert, S. Roth, Z.F. Zhang, L. Schultz, W.H. Wang, Mechanical behavior of Fe65.5Cr4Mo4Ga4P12C5B5.5 bulk metallic glass, Intermetallics 13 (2005) 764–769.
[30] A. Inoue, B.L. Shen, A.R. Yavari, A.L. Greer, Mechanical properties of Fe-based bulk glassy alloys in Fe-B-Si-Nb and Fe-Ga-P-C-B-Si systems, J. Mater. Res. 18 (2003) 1487–1492.
[31] X.J. Gu, S.J. Poon, G.J. Shiflet, Mechanical properties of iron-based bulk metallic glasses, J. Mater. Res. 22 (2007) 344–351.
[32] H.L. Peng, L. Hu, L.J. Li, L.Y. Zhang, X.L. Zhang, Evolution of the microstructure and mechanical properties of powder metallurgical high-speed steel S390 after heat treatment, J. Alloy Compd. 740 (2018) 766–773.
[33] W.J. Xi, H.J. Wang, J. Li, C.L. Shi, A NiAl- and TiC-reinforced Fe-based nanocomposite prepared by the rapid-solidification thermite process, Mater. Sci. Eng. A 541 (2012) 166–171.
[34] B. AlMangour, D. Grzesiak, T. Borkar, J.M. Yang, Densification behavior, microstructural evolution, and mechanical properties of TiC/316L nanocomposites fabricated by selective laser melting, Mater. Des. 138 (2018) 119–128.
[35] J.M. Kim, J.S. Park, Microstructure and mechanical properties of TiC nanoparticle-reinforced iron-matrix composites, Strength Mater. 46 (2014) 177–182.
[36] M. Ziemnicka-Sylwester, L. Gai, S.J. Miura, Effect of (Ti:B) atomic ratio on mechanical properties of TiB2-Fe composites “in situ” fabricated via Self-propagating High-temperature Synthesis, Mater. Des. 69 (2015) 1–11.
[37] I. Sulima, Role of boron addition on the consolidation and properties of steel composites prepared by SPS, Bull. Mater. Sci. 38 (2015) 1831–1841.
[38] B. AlMangour, D. Grzesiak, J.M. Yang, Rapid fabrication of bulk-form TiB2/316L stainless steel nanocomposites with novel reinforcement architecture and improved performance by selective laser melting, J. Alloy Compd. 680 (2016) 480–493.
[39] J. Liu, W.P. Chen, L. Chen, Z.B. Xia, H.Q. Xiao, Z.Q. Fu, Microstructure and mechanical behavior of spark plasma sintered TiB2/Fe-15Cr-8Al-20Mn composites, J. Alloy Compd. 747 (2018) 886–894.